

# ACCEPTED VERSION

Carman Yeung, Ching Tai Ng

**Time-domain spectral finite element method for analysis of torsional guided waves scattering and mode conversion by cracks in pipes**

Mechanical Systems and Signal Processing, 2019; 128:305-317

© 2019 Elsevier Ltd. All rights reserved.

This manuscript version is made available under the CC-BY-NC-ND 4.0 license

<http://creativecommons.org/licenses/by-nc-nd/4.0/>

Final publication at: <http://dx.doi.org/10.1016/j.ymssp.2019.04.013>

## PERMISSIONS

<https://www.elsevier.com/about/policies/sharing>

Accepted Manuscript

Authors can share their [accepted manuscript](#):

24 Month Embargo

### After the embargo period

- via non-commercial hosting platforms such as their institutional repository
- via commercial sites with which Elsevier has an agreement

In all cases [accepted manuscripts](#) should:

- link to the formal publication via its DOI
- bear a CC-BY-NC-ND license – this is easy to do
- if aggregated with other manuscripts, for example in a repository or other site, be shared in alignment with our [hosting policy](#)
- not be added to or enhanced in any way to appear more like, or to substitute for, the published journal article

**3 June 2022**

<http://hdl.handle.net/2440/121200>

**Journal article:**

Carman Yueng, Ching Tai Ng. (2019). Time-domain spectral finite element method for analysis of torsional guided waves scattering and mode conversion by cracks in pipes. *Mechanical Systems and Signal Processing*, 128:305-317.

# **Time-domain Spectral Finite Element Method for Analysis of Torsional Guided Waves Scattering and Mode Conversion by Cracks in Pipes**

Carman Yeung and Ching Tai Ng\*

School of Civil, Environmental & Mining Engineering, The University of Adelaide, 5005 SA,  
Australia

## **Abstract**

This paper presents a computational efficient time-domain spectral finite element method (SFEM) and a crack model to take into account guided wave propagation, scattering and mode conversion in pipes. The proposed SFEM couples torsional and flexural motions of guided waves. A cracked element is proposed to predict the scattering and mode conversion effect of guided wave interaction with the crack in the pipes. The proposed SFEM and cracked element are verified by 3D finite element and experimental data. The results show that the proposed SFEM is able to predict the torsional guided wave propagation, scattering and mode conversion accurately. A series of numerical and experimental case studies are carried out to investigate the effect of the crack size on the scattering and mode converted guided waves. The findings of the study provide physical insights into the guided wave scattering and mode conversion and further advance the development of damage detection using guided waves.

**Keywords:** Guided waves, spectral finite element method, scattering, mode conversion, crack, pipe, torsional wave, circular waveguide

---

\* Corresponding author: [alex.ng@adelaide.edu.au](mailto:alex.ng@adelaide.edu.au)

## 1. Introduction

Structural health monitoring (SHM) plays an important role in assessing condition of structures in many engineering fields, such as civil, mechanical and, oil and gas industry. Successful applications of SHM could help engineers achieve cost-effective management of infrastructure and avoid catastrophic failure by providing an early detection of defects. This improves the safety and sustainability of the infrastructures. In the last two decades, different damage detection techniques have been developed [1,2], for example, non-destructive evaluation (NDE) techniques, such as conventional ultrasonic techniques, eddy current, infrared thermography, vibration-based techniques [3], and guided wave techniques [4-6].

### *1.1. Damage detection in circular waveguides*

Guided waves are elastic waves travelling in solid materials and the wave propagation characteristics depend on boundary conditions of structures. Based on the wave propagation characteristics, guided waves can be categorized as different types of waves, e.g. shear horizontal wave [7], torsional wave [8], Rayleigh wave [9] and Lamb wave [10]. Shear horizontal wave refers to the wave with propagation direction perpendicular to the particle motion. Torsional wave is shear horizontal wave propagation in pipes with propagation direction aligning with the longitudinal axis [11]. Rayleigh wave is a type of surface wave and has been commonly used in the literature [12]. Lamb wave is elastic wave propagation in thin-walled structures, such as thin plates [13,14]. There are two common types of waveguides, one-dimensional (1D) waveguides, such as beams, rods and pipes [15,16], and two-dimensional (2D) waveguides, such as plates and shells [17-19].

### *1.2. Damage detection in circular waveguides*

Pipelines are commonly used in different industrial sectors and pipes are usually treated as circular waveguide in the context of wave propagation. Defects in pipe is a considerable problem for oil,

chemical or other pipeline transportation industries [20]. When pitting defects and corrosion appear in the structures, there is higher chance of structural failure. The structural safety inspection becomes more difficult if external surface of the pipes has a layer of protective material, such as bitumen. For example, if flaw pipelines are buried as underground utilities, this will cause a significant inconvenient to public. The study of Ahmad *et al.* [21] showed that pipes were frequently embedded in the soil with insulated coatings. Angani *et al.* [22] studied the use of eddy current to inspect the defects in pipelines but the inspection can be carried out in a limited area only. It is impractical to use inspection methods that require direct access to the pipes since the associated cost of removing the insulation is unpredictably high.

Damage detection using torsional guided wave in circular waveguide has been demonstrated that it can provide long-range inspection. Due to the non-dispersive characteristic of fundamental torsional wave  $T(0,1)$ , the use of this wave mode has practical significance in structural integrity assessment [23,24]. Løvstad and Cawley [25] proposed to use torsional guided wave to detect defects in pipes. They concluded that the damage inspection can cover ten meters of pipe section and the long-range testing is not affected by the pipe coatings. Eybpoosh *et al.* [26] further investigated the application of guided waves for damage detection of pipelines under varying environmental and operational conditions. The study of circular waveguides can further advance damage detection techniques for the pipes using guided waves.

### *1.3. Numerical method for wave propagation simulations*

Different methods for modelling wave propagation phenomena in structures have been developed in the literature. Numerical methods have been used for simulating guided wave propagation in different types of structures [27]. Finite difference method (FDM) is defined on regular grids, which is efficient for large scale simulations. But it is not capable of handling wave simulation when there are changes in material property and geometry of the structures [28]. The boundary element method (BEM) is capable for modelling small surface/volume ratio. By contrast, it is not computational efficient for

modelling large structures [29]. Finite strip element (FSE) has low discretisation level, but it is not suitable to model geometrically complex structures [30]. Finite element method (FEM) is extensively used in modelling complex geometries. However, it is computationally expensive for wave propagation simulations [31,32].

The main difference of the spectral finite element method (SFEM) and FEM is that SFEM uses a higher-order interpolation with specific quadrature formulae [33,34]. Less arithmetic operations can be achieved since the mass matrix is diagonalized by using particular formulations. In SFEM, the use of high-order shape functions allows simulation of wave propagation using less elements to achieve the similar accuracy of FEM. Therefore, SFEM is capable of simulating wave propagation and has better convergent rate than FEM. The research on SFEM for wave propagation has been conducted since the early 1990s [35]. Most of the studies in the early stage started by employing Chebyshev–Gauss–Lobatto (CGL) nodes to simulate acoustic waves [36]. Gauss–Lobatto–Legendre (GLL) nodes, which have similar capability of CGL, were then introduced to model elastic waves.

Other higher-order numerical simulation methods, such as SFEM, p-version of FEM (p-FEM) and isogeometric analysis (IGA) [37-39], have been applied for wave propagation analysis in order to reduce the computational costs. The selection of basis functions is the difference between these three numerical methods. The SFEM uses the Lagrange interpolation polynomials. The normalized integrals of the Legendre polynomials are deployed as the basis functions of the p-FEM. The IGA employs NURBS-based (Nonuniform Rational B-splines) basis functions. Among these numerical simulation methods, all degrees-of-freedom (DoFs) in SFEM keep the physical meaning for their geometrical nodes so that the post-processing of the simulation results is more convenient.

This paper presents a cracked element to take into account the mode conversion effect of guided waves in pipe using time-domain SFEM. A comprehensive study of guided waves in pipes using time-domain SFEM is conducted and the results are verified by 3D FEM and experimental data. The findings of this study gain physical insights into the guided wave scattering and mode conversion

at the crack in pipes and can further advance the development of damage detection methods using guided wave.

The structure of this paper is as follow. Section 2 presents the time-domain SFEM and the proposed crack model. The properties and selection of the guided wave mode are discussion in Section 3. Section 4 presents a comparison of the results between SFEM and 3D FEM. This section validates the proposed cracked model for the time-domain SFEM, and also investigates the scattering and mode conversion effect of guided waves at the crack in pipes. The proposed time-domain SFEM is then validated by experimental data in Section 5. Finally, conclusions are drawn in Section 6.

## 2. Methodology

### 2.1. Coupling of torsional and flexural motions for circular waveguide

In this study, the time-domain SFEM for pipe is developed based on the elementary rod theory [40] and Timoshenko beam theory [15]. Fig. 1 shows a schematic diagram of a pipe element with a crack. Timoshenko beam theory considers the vertical/horizontal direction and the corresponding shear deformation defect. The torsional motion is modelled by the elementary rod theory based on Saint-Venant principle. The governing equations for coupling torsional and flexural motions of circular waveguide are [41]

$$GJ \frac{\partial^2 \theta}{\partial x^2} + F_\theta(x, t) = \rho I_o \ddot{\theta} \quad (1)$$

$$K_1^{Tim} GA \frac{\partial}{\partial x} \left( \frac{\partial v}{\partial x} - \varphi \right) = \rho A \ddot{v} - F_v(x, t)$$

$$EI \frac{\partial^2 \varphi}{\partial x^2} + K_1^{Tim} GA \left( \frac{\partial v}{\partial x} - \varphi \right) = K_2^{Tim} \rho I \ddot{\varphi} \quad (2)$$

where  $\theta$  is the torsional motion,  $v$  is the displacement along y-axis, and  $\varphi$  is the rotation about z-axis (Fig. 1). The mass density and cross-section area of the pipe are denoted by  $\rho$  and  $A$ , respectively.  $I$ ,  $J$  and  $I_o$  are the second moment of inertia about z-axis, the polar moment of inertia, and the second moment of inertia about x-axis, respectively.  $E$  is Young's modulus and  $G$  is shear modulus. The

influence of group velocity is controlled by  $K_1^{\text{Tim}}$  and  $K_2^{\text{Tim}}$  [42]. The parameters for torsional guided waves are  $K_1^{\text{Tim}} = 0.28$  and  $K_2^{\text{Tim}} = 45K_1^{\text{Tim}}/\pi^2$ .  $F_\theta$  and  $F_v$  represent the function for the external torsional and vertical excitation, respectively.

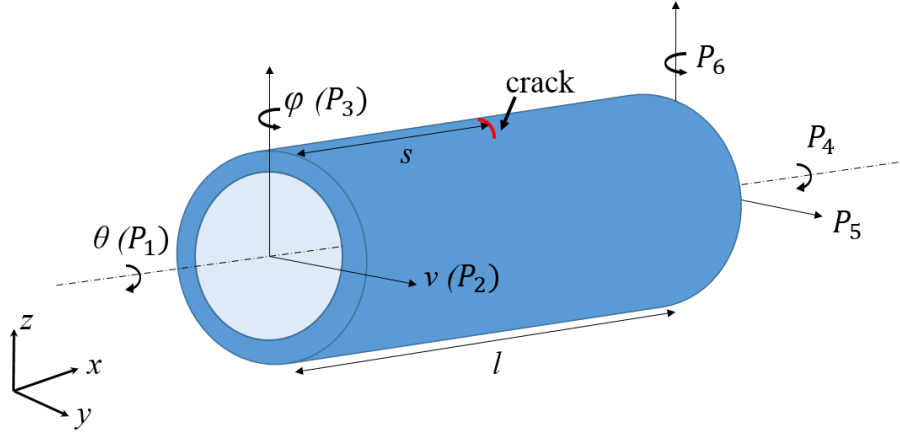


Fig. 1 Schematic diagram of a pipe with a surface crack

## 2.2. Time-domain spectral finite element method

The wave propagation can be represented by ordinary differential equation [43]

$$\mathbf{M}\ddot{\mathbf{u}} + \mathbf{C}\dot{\mathbf{u}} + \mathbf{K}\mathbf{u} = \mathbf{F}(t) \quad (3)$$

where  $\mathbf{M}$  is the global mass matrix,  $\mathbf{C}=\eta\mathbf{M}$  is the global damping matrix with damping parameter  $\eta$  [44,45].  $\mathbf{K}$  is the global stiffness matrix and  $\mathbf{F}(t)$  is the global force vector.  $\mathbf{u}$ ,  $\dot{\mathbf{u}}$  and  $\ddot{\mathbf{u}}$  denote the time-domain displacement, velocity and acceleration vector, respectively. The local mass matrix  $\mathbf{m}$ , local stiffness matrix  $\mathbf{k}$ , and local load vector  $\mathbf{f}$  are

$$\mathbf{m} \approx \sum_{i=1}^n w_i \mathbf{N}_e(\xi_i)^T \boldsymbol{\mu} \mathbf{N}_e(\xi_i) \det(\mathbf{J}(\xi_i)) \quad (4)$$

$$\mathbf{k} \approx \sum_{i=1}^n w_i \mathbf{B}_e(\xi_i)^T \mathbf{D} \mathbf{B}_e(\xi_i) \det(\mathbf{J}(\xi_i)) \quad (5)$$

$$\mathbf{f} \approx \sum_{i=1}^n w_i \mathbf{N}_e(\xi_i)^T \mathbf{f}(\xi_i) \det(\mathbf{J}(\xi_i)) \quad (6)$$



where  $n$  is the node number in the element.  $\mathbf{J} = \frac{\partial x}{\partial \xi}$  is the Jacobian function used to assign the local coordinate to the global domain.  $\mathbf{f}(\xi_i)$  is the external force and  $\xi_i$  is the local coordinate of node  $i$  in the element.

In this study, GLL nodes are used as local nodes in each element [46]. The nodes are taken as roots of the equation

$$(1 - \xi_i^2)L'_{n-1}(\xi_i) = 0 \quad \text{for} \quad \xi_i \in [-1,1] \text{ and } i \in 1, \dots, n \quad (7)$$

where  $L'_{n-1}$  denotes the first derivative of the  $(n-1)$ th order Legendre polynomial. The weighting function of the corresponding GLL point  $\xi_i$  is

$$w_i = \frac{2}{n(n-1)(L_{n-1}(\xi_i))^2} \quad (8)$$

The diagonal form of mass matrix is achieved due to the Kronecker property of the shape function. It can be solved by the central difference scheme. The shape function matrix  $\mathbf{N}_e$  in equation (4) is defined as

$$\mathbf{N}_e = \mathbf{N} \otimes \mathbf{I} \quad (9)$$

where  $\otimes$  is the Kronecker product,  $\mathbf{I}$  is a  $3 \times 3$  identity matrix, and  $\mathbf{N} = [N_1(\xi), \dots, N_n(\xi)]$ . The spectral shape function  $N_i(\xi)$  for node  $i$  is defined as

$$N_i(\xi) = \prod_{k=1, k \neq i}^n \frac{\xi - \xi_k}{\xi_i - \xi_k} \quad (10)$$

In the SFEM, each node consists of three DoFs. The displacement fields are

$$\begin{bmatrix} \theta^e \\ v^e \\ \varphi^e \end{bmatrix} = \sum_{i=1}^n \begin{bmatrix} N_i(\xi) & 0 & 0 \\ 0 & N_i(\xi) & 0 \\ 0 & 0 & N_i(\xi) \end{bmatrix} \begin{bmatrix} q_\theta^e(\xi_i) \\ q_v^e(\xi_i) \\ q_\varphi^e(\xi_i) \end{bmatrix} \quad (11)$$

The strain-displacement operator  $\mathbf{B}$  is a  $3 \times 3$  matrix and is defined as

$$\mathbf{B} = \begin{bmatrix} E_{Tor} & 0 \\ 0 & E_{Tim} \end{bmatrix} \mathbf{N} \quad (12)$$

$$\text{where } E_{Tor} = \left[ \frac{1}{J} \frac{\partial}{\partial \xi} \right], \quad E_{Tim} = \begin{bmatrix} \frac{1}{J} \frac{\partial}{\partial \xi} & -1 \\ 0 & \frac{1}{J} \frac{\partial}{\partial \xi} \end{bmatrix}, \quad (13)$$

$E_{Tor}$  and  $E_{Tim}$  are differential operator for elementary rod theory and Timoshenko beam theory, respectively.  $\mathbf{D}$  and  $\boldsymbol{\mu}$  are  $3 \times 3$  stress-strain matrix and  $3 \times 3$  mass density matrix, respectively. They are defined as

$$\mathbf{D} = \begin{bmatrix} D_{Tor} & 0 \\ 0 & D_{Tim} \end{bmatrix} \quad (14)$$

$$\text{where } D_{Tor} = [GJ], \quad D_{Tim} = \begin{bmatrix} K_1^{Tim} GA & 0 \\ 0 & EI \end{bmatrix} \text{ and} \quad (15)$$

$$\boldsymbol{\mu} = \begin{bmatrix} \mu_{Tor} & 0 \\ 0 & \mu_{Tim} \end{bmatrix} \quad (16)$$

$$\mu_{Tor} = [\rho I_o], \quad \mu_{Tim} = \begin{bmatrix} \rho A & 0 \\ 0 & K_2^{Tim} \rho I \end{bmatrix} \quad (17)$$

### 2.3. Cracked element modelling

This section presents the formulation for the cracked element for pipes in SFEM. The analysis of cracks in circular shape structural elements has been reported in the literature [47,48]. The following derivation of the cracked element is an extension from the work of Darpe *et al.* [49]. Consider a circular waveguide with hollow cross-section at the crack location as shown in Fig. 2.  $D$  and  $d$  are outer and inner diameter of the pipe, respectively, and  $a$  is crack depth.

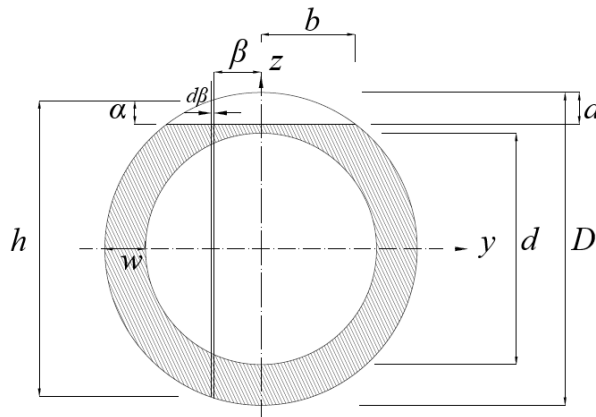


*Fig. 2 Cross-section of circular waveguide at the crack location*

The notations  $h$ ,  $\beta$  and  $\alpha$  in Fig. 2 are for calculating the flexibility matrix and are used in equation (31).  $h$  and  $\alpha$  in equations (18) and (19) are linked by  $D$ ,  $a$  and  $y$ .

$$h = 2\sqrt{\left(\frac{D}{2}\right)^2 - y^2} \quad (18)$$

$$\alpha = \frac{h}{2} - \left(\frac{D}{2}\right) + a \quad (19)$$

The proposed cracked element is a two-node element having three DoFs ( $\theta$ ,  $v$  and  $\varphi$ ) at each node. Fig. 3 shows the discretization of a circular waveguide with a two-node cracked element. Due to the existence of crack, the stiffness properties in the cracked element are different to the uncracked element. The modified stiffness matrix takes into account the mode coupling effect. So the guided wave scattering and mode conversion effect can be simulated by the time-domain SFEM.

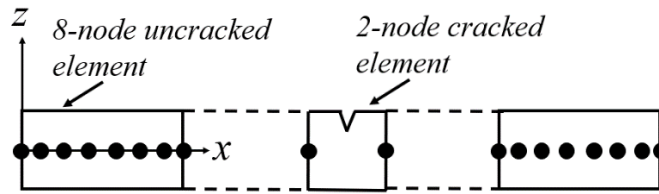


*Fig. 3 Discretization of a circular waveguide with a cracked element*

The modified stiffness matrix can be obtained from the local flexibility matrix since they are interrelated to each other. By using Castiglino's theorem,

$$Q_i = \frac{\partial U}{\partial P_i} \quad \text{for} \quad i \in 1,2,3 \quad (20)$$

where  $Q_i$  and  $P_i$  are the displacement and load along the  $i$ th coordinate at the first node, respectively.  $P_1, P_2$  and  $P_3$  are torsional moment, shear force and bending moment, respectively.  $U$  is the total strain energy, which can be separated from the strain energy of the uncracked ( $U^u$ ) and cracked ( $U^c$ ) elements. Equation (20) can be expressed as

$$Q_i = Q_i^u + Q_i^c = \frac{\partial U^u}{\partial P_i} + \frac{\partial U^c}{\partial P_i} \quad (21)$$

The strain energy with the uncracked element is written as

$$U^u = \frac{1}{2} \int \left[ \frac{P_1^2}{GI_0} + \frac{kP_2^2}{GA} + \frac{(sP_2 + P_3)^2}{EI} \right] dx \quad (22)$$

where  $k$  is the shear coefficient [50]. The individual displacement of the uncracked elements is given by the following expression

$$\begin{aligned} Q_1^u &= \frac{lP_1}{GI_0} \\ Q_2^u &= \left( \frac{kl}{GA} + \frac{l^3}{3EI} \right) P_2 + \frac{l^2}{2EI} P_3 \\ Q_3^u &= \frac{l}{EI} P_3 + \frac{l^2}{2EI} P_2 \end{aligned} \quad (23)$$

The strain energy due to crack  $U^c$  can be calculated by fracture mechanics, which is defined in the form

$$U^c = \int_A R(A) dA \quad (24)$$

where  $R(A)$  is the strain energy density function. The function is defined as

$$R(A) = \frac{1}{E} [(\sum_{i=1}^3 K_{Ii})^2 + (\sum_{i=1}^3 K_{IIi})^2 + m(\sum_{i=1}^3 K_{IIIi})^2] \quad (25)$$

where  $m = 1 + \nu$ .  $\nu$  is the Poisson ratio.  $K_{Ii}$ ,  $K_{IIi}$  and  $K_{IIIi}$  are the stress intensity factors (SIF) for opening mode, sliding mode and shearing mode of crack displacement, respectively. The stress intensity factors for different opening modes are

SIF for opening mode,

$$\begin{aligned} K_{I3} &= \frac{(P_3 + sP_2)\beta}{\pi/64(D^4 - d^4)} \sqrt{\pi\alpha} F_1 \\ K_{I1} &= K_{I2} = 0 \end{aligned} \quad (26)$$

SIF for sliding mode,

$$\begin{aligned} K_{II1} &= \frac{P_1\beta}{\pi/32(D^4 - d^4)} \sqrt{\pi\alpha} F_{II} \\ K_{II2} &= K_{II3} = 0 \end{aligned} \quad (27)$$

SIF for shearing mode,

$$\begin{aligned}
K_{III1} &= \frac{2P_1 h}{\pi/32(D^4 - d^4)} \sqrt{\pi \alpha} F_{III} \\
K_{III2} &= \frac{P_2 k}{\pi(D/2^2 - d/2^2)} \sqrt{\pi \alpha} F_{III} \\
K_{III3} &= 0
\end{aligned} \tag{28}$$

The calculations of  $F_I$ ,  $F_{II}$  and  $F_{III}$  are depicted as

$$\begin{aligned}
F_I &= \sqrt{\frac{2h}{\pi \alpha} \tan\left(\frac{\pi \alpha}{2h}\right)} \frac{0.752 + 2.02\left(\frac{\alpha}{h}\right) + 0.37\left[1 - \sin\left(\frac{\pi \alpha}{2h}\right)\right]^3}{\cos\left(\frac{\pi \alpha}{2h}\right)} \\
F_{II} &= \frac{1.122 - 0.561\left(\frac{\alpha}{h}\right) + 0.085\left(\frac{\alpha}{h}\right)^2 + 0.18\left(\frac{\alpha}{h}\right)^3}{\sqrt{1 - \left(\frac{\alpha}{h}\right)}} \\
F_{III} &= \sqrt{\frac{2h}{\pi \alpha} \tan\left(\frac{\pi \alpha}{2h}\right)}
\end{aligned} \tag{29}$$

Substitute the equations (26)-(29) into equations (24) and (25),  $Q_i^c$  is simplified to

$$\begin{aligned}
Q_1^c &= (I_{g1} + I_{g2}) P_1 + I_{g5} P_2 \\
Q_2^c &= I_{g5} P_1 + s(sP_2 + P_3) I_{g3} + I_{g4} P_2 \\
Q_3^c &= (sP_2 + P_3) I_{g3}
\end{aligned} \tag{30}$$

where  $I_{g1}$ ,  $I_{g2}$ ,  $I_{g3}$ ,  $I_{g4}$  and  $I_{g5}$  in equation (30) are defined as

$$\begin{aligned}
I_{g1} &= \int_A \frac{8\alpha \beta^2 F_{II}^2}{\pi E (D/2^4 - d/2^4)^2} dA & I_{g4} &= \int_A \frac{2mk^2 \alpha (D/2^2 + d/2^2)^2 F_{III}^2}{\pi E (D/2^4 - d/2^4)^2} dA \\
I_{g2} &= \int_A \frac{2m\alpha h^2 F_{III}^2}{\pi E (D/2^4 - d/2^4)^2} dA & I_{g5} &= \int_A \frac{2mk\alpha h (D/2^2 + d/2^2) F_{III}^2}{\pi E (D/2^4 - d/2^4)^2} dA \\
I_{g3} &= \int_A \frac{32\alpha \beta^2 F_I^2}{\pi E (D/2^4 - d/2^4)^2} dA
\end{aligned} \tag{31}$$

By combining equations (23) and (30), the total displacement  $Q_i$  from equation (21) can be expressed in a matrix form as

$$[Q_i] = \mathbf{G}[P_i] \quad \text{for} \quad i \in 1, \dots, 6 \tag{32}$$

The flexibility matrix  $\mathbf{G}$  is defined as

$$\mathbf{G} = \begin{bmatrix} g_{11} & g_{12} & g_{13} \\ g_{21} & g_{22} & g_{23} \\ g_{31} & g_{32} & g_{33} \end{bmatrix} \quad (33)$$

where

$$\begin{aligned} g_{11} &= \frac{l}{GI_0} + I_{g1} + I_{g2} & g_{12} &= g_{21} = I_{g5} \\ g_{22} &= \frac{kl}{GA} + \frac{l^3}{3EI} + I_{g4} + s^2 I_{g3} & g_{13} &= g_{31} = 0 \\ g_{33} &= \frac{l}{EI} + I_{g3} & g_{23} &= g_{32} = \frac{l^2}{2EI} + s I_{g3} \end{aligned}$$

Considering the static equilibrium of the cracked element, the flexibility matrix  $\mathbf{G}$  can convert to the stiffness matrix by transformation matrix  $\mathbf{T}$ . The orders of the DoFs in this two-node element are presented by the subscripts  $q$ .

$$\{q_i\}^T = \mathbf{T}\{q_j\}^T \quad \text{for} \quad i \in 1, \dots, 6 \quad \& \quad j \in 1, 2, 3 \quad (34)$$

$$\mathbf{T}^T = \begin{bmatrix} 1 & 0 & 0 & -1 & 0 & 0 \\ 0 & 1 & 0 & 0 & -1 & -l \\ 0 & 0 & 1 & 0 & 0 & -1 \end{bmatrix} \quad (35)$$

The stiffness matrix for the cracked element can be calculated by flexibility matrix as

$$\mathbf{k}_c = \mathbf{T}\mathbf{G}^{-1}\mathbf{T}^T \quad (36)$$

It should be noted that the global stiffness matrix  $\mathbf{K}$  in equation (3) is assembled by the local uncracked stiffness matrix  $\mathbf{k}$  and the local cracked stiffness matrix  $\mathbf{k}_c$ . So the proposed time-domain SFEM can take into account the torsional-flexural coupling effect in modelling the guided waves scattering and mode conversion at the crack on pipes.

### 3. Wave Mode Selection

Dispersion curves are a fundamental indication for the selection of optimal excitation mode and excitation frequency in damage detection. Fig. 4(a) shows the group velocity dispersion curves

of longitudinal, torsional and flexural modes in pipes, which are marked as  $L(m,n)$ ,  $T(m,n)$  and  $F(m,n)$ , respectively. ‘ $m$ ’ and ‘ $n$ ’ are integers, which represent the harmonic order of circumferential variation and a sequential number of modes of each category, respectively [51]. Torsional modes are axially symmetric, while the flexural modes are axisymmetric. Most of the wave modes are dispersive, which limits the wave propagation distance. But the fundamental torsional mode  $T(0,1)$  is non-dispersive, which is useful for damage detection in pipes. So torsional  $T(0,1)$  mode is adopted as incident wave in this study. Fig 4(b) show the group velocity calculated by SFEM and DISPERSE. Red dashed line and blue solid line denote the group velocities of  $T(0,1)$  mode and  $F(1,1)$  mode from a commercial software DISPERSE [52]. The markers represent the group velocities calculated from the proposed SFEM.

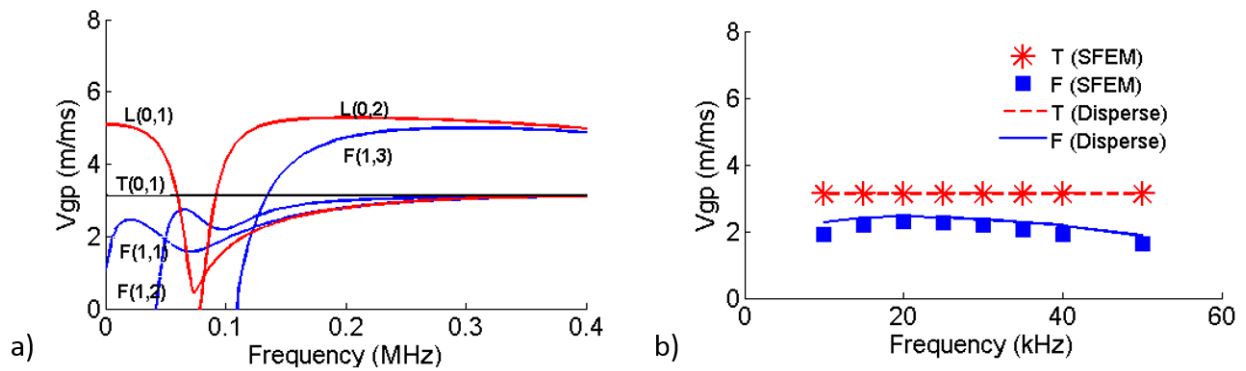


*Fig. 4 (a) Group velocity dispersion curves obtained from DISPERSE and (b) group velocities calculated by the proposed SFEM and DISPERSE*

A 1m long aluminium pipe is modelled using the proposed time-domain SFEM method. The density and Poisson's ratio are 70GPa, 2700kg/m<sup>3</sup> and 0.3, respectively. The wall thickness and outer diameter of the pipe are 3mm and 25mm, respectively. A crack is modelled at the middle of the pipe using the proposed cracked element. Eight GLL nodes with 0.01m long spectral elements were used to model the pipe. The central difference method was applied to solve the ordinary differential equation (Eq. 3). The time step was  $1 \times 10^{-7}$  s to ensure the solution to be converged. The torsional

guided wave  $T(0,1)$  was generated by applying nodal rotation about x-axis at the left end of the pipe to generate the torsional guided waves. The excitation signal was a 50kHz 5-cycle sinusoidal tone burst modulated by a Hanning window.

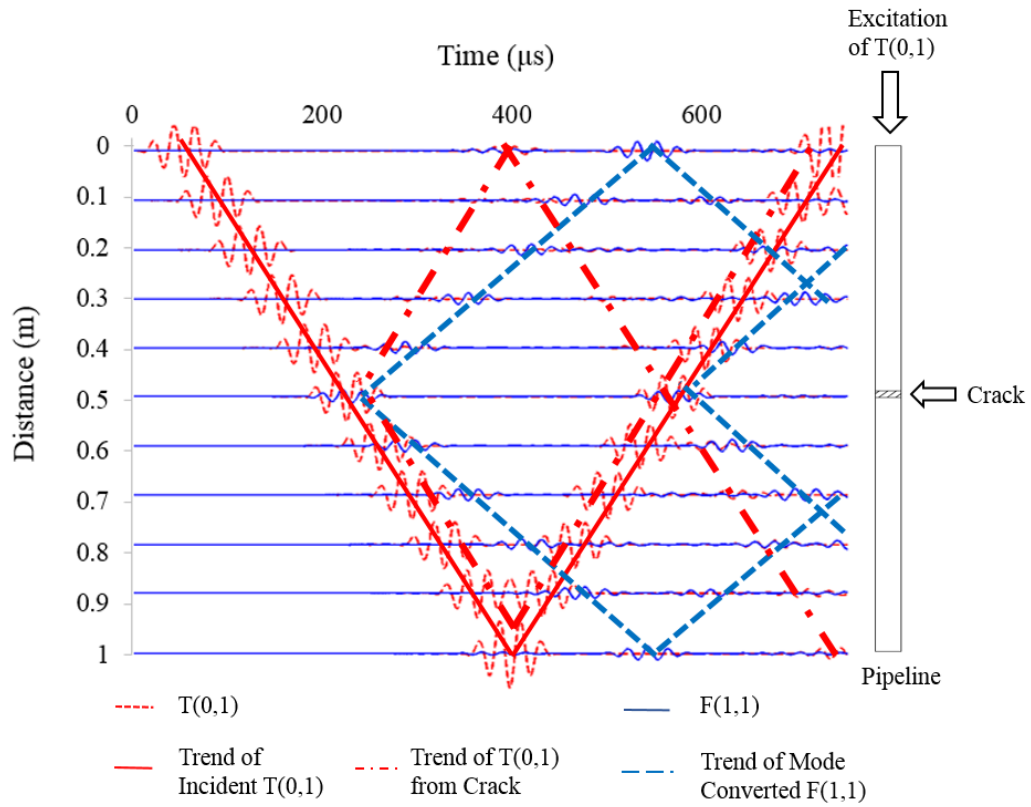


*Fig. 5 Wave propagation of torsional wave and mode converted flexural wave*

The propagation of the  $T(0,1)$  wave and mode converted ( $F(1,1)$ ) wave due to the crack is shown in Fig. 5. Torsional wave and flexural wave are indicated by red dashed line and blue solid line, respectively. The trend lines for different wave modes are shown in Fig. 5. The propagation velocities for  $T(0,1)$  wave and  $F(1,1)$  wave are different. The group velocity for the  $T(0,1)$  and  $F(1,1)$  wave are  $3130 \text{ m/s}$  and  $1900 \text{ m/s}$ , respectively. The mode converted  $F(1,1)$  wave first appears at the middle of the pipe because of the presence of the crack. Since the incident  $T(0,1)$  and the  $T(0,1)$  reflected from



the crack have the same group velocity, the slopes of their trend lines are in parallel as shown in Fig. 5.

#### 4. Validation by Three-dimensional finite element model

A 3D finite element model of the same aluminium pipe with the same crack and incident wave used in Section 4 was created by ABAQUS and used to validate the accuracy of the proposed SFEM. 3D eight-node brick elements (C3D8R) [53] were used to model the pipe and the maximum size of the element used in the model is 0.8mm, which ensures there are at least 20 elements per wavelength for both  $T(0,1)$  and  $F(1,1)$  modes [54]. The thickness of the elements is 0.6mm so that there are five elements across the thickness of pipe wall. A notch having 1mm width and different depths was modelled at the middle of the pipe by removing the elements. The incident  $T(0,1)$  wave was generated by applying point loads at four edges of the circumference at the pipe end. The excitation signal is the same as the signal used in Section 3. Fig. 6 shows the notch modelled at the middled of the pipe, which is modelled asymmetrically about the longitudinal axis.

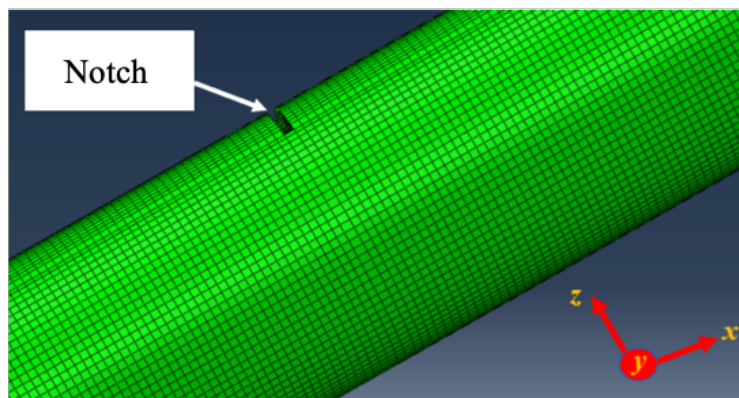


*Fig. 6 Notch at the middle of the pipe in the 3D finite element model*

Fig. 7 compares the wave signals simulated by SFEM and 3D FEM. The signals were obtained at 0.3m away from the excitation location and the crack depth is 2.01mm. Fig. 7a shows the deformation in torsional DoF ( $\theta$ ), which contains the information of the incident wave  $T(0,1)$  wave and  $T(0,1)$  wave due to the crack (T-T wave). Fig. 7b shows that the deformation in vertical DoF ( $v$ ), which is the mode converted  $F(1,1)$  wave due to the crack (T-F wave). There is good agreement between the results calculated by SFEM and 3D FEM. The incident  $T(0,1)$ , T-T wave from the crack and the mode converted T-F wave from the crack are labelled in Fig. 6.

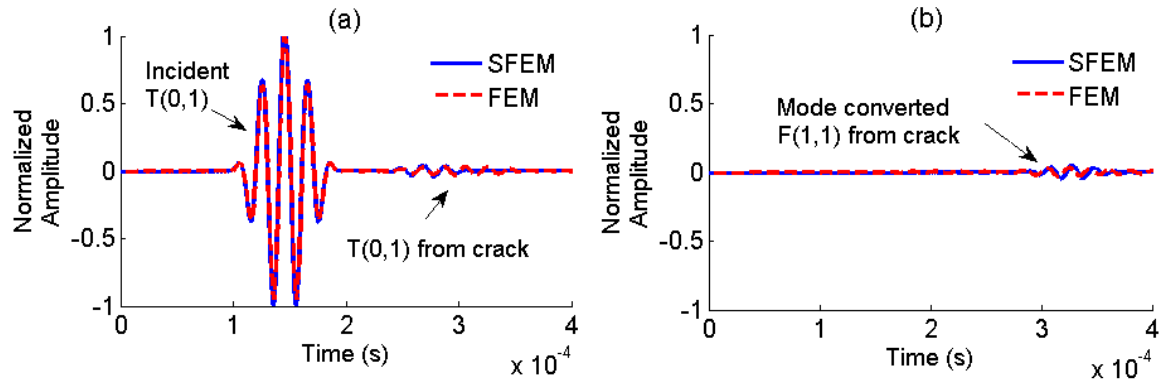


Fig. 7 Signals simulated by SFEM and 3D FEM (a) torsional DoF and (b) vertical DoF

A series of parametric studies were carried out using the SFEM and 3D FEM to investigate the characteristics of T-T wave and mode converted T-F wave due to the crack. Different crack depths were simulated using the SFEM and 3D FEM the results are shown in Figs. 8 and 9. These two figures show the relationship between the wave amplitudes and the crack depth against pipe wall thickness ratios. Fig. 8 shows the reflected T-T wave and the reflected T-F wave due to mode conversion effect at the crack and Fig. 9 shows the corresponding transmitted waves.

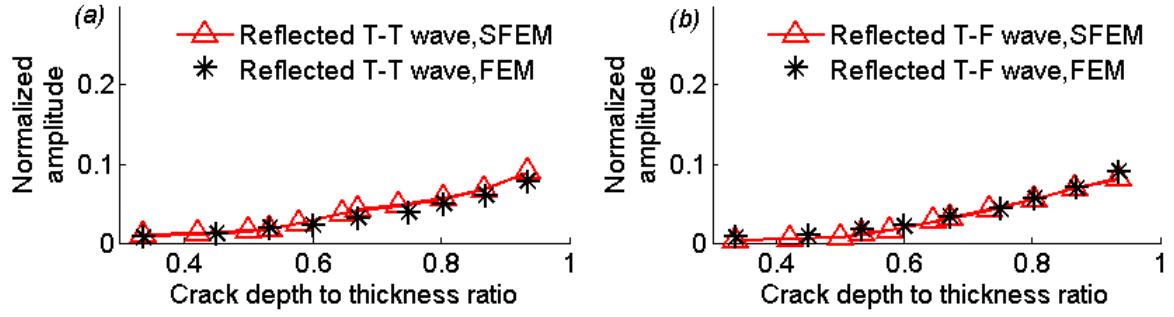


Fig. 8 Normalized amplitude of a) the reflected T-T wave and b) the reflected T-F wave as a function of crack depth to thickness ratio for the results simulated by SFEM and 3D FEM

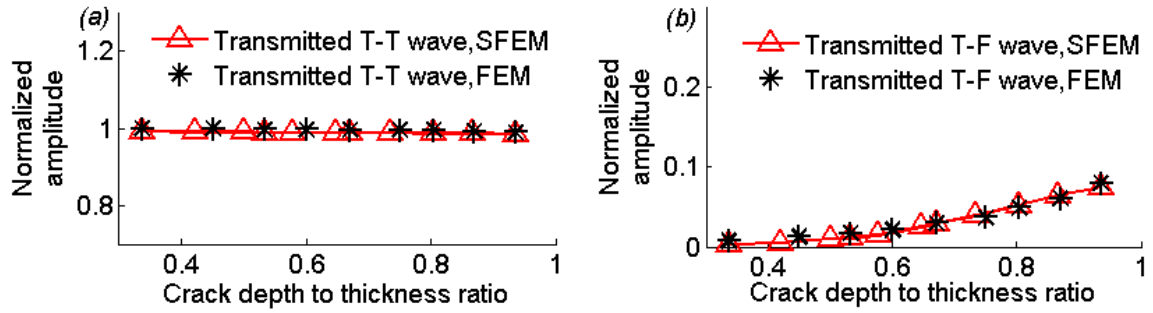
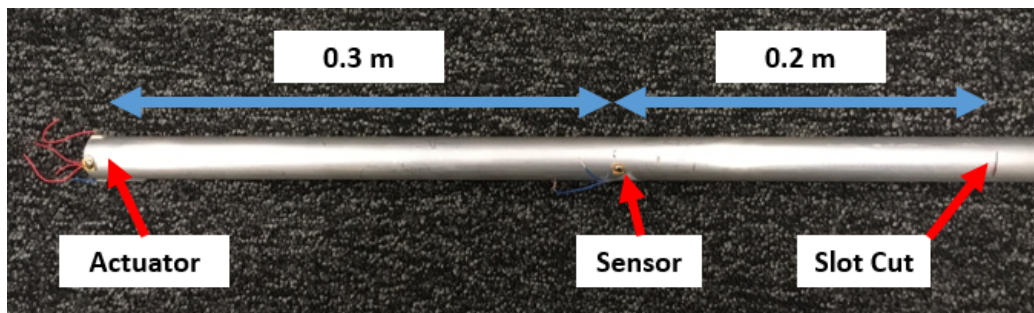


Fig. 9 Normalized amplitude of a) the transmitted T-T wave and b) the transmitted T-F wave as a function of crack depth to thickness ratio for the results simulated by SFEM and 3D FEM

The transmitted and reflected waves are generated due to the interaction of the incident guided wave at the crack. The transmitted guided wave propagates toward the measurement point located at  $x = 0.7m$ . Meanwhile, the reflected wave travels back from the crack to the measurement point located at  $x = 0.3m$ . The amplitude of the measured data was normalized to allow comparison. The generation of mode converted wave is due to the asymmetric crack. The transmitted wave is the superposition of scattered wave and incident wave, while the reflected waves only contain scattered waves. This explains why the transmission signal is much larger than the wave reflected from the crack. The amplitude of transmitted T-T wave slightly decreases with crack depth to thickness ratio because part of the energy is transferred to the other wave mode. As shown in Figs. 8 and 9, there is good agreement between the results simulated by SFEM and 3D FEM.

## 5. Experimental Setup for Actuating and Sensing Torsional Guided Wave

A 1m long aluminium pipe with an outer diameter of 25mm and pipe wall thickness of 3mm was used to further validate the accuracy of the proposed time-domain SFEM. A slot cut of 1mm width was created at the middle of the pipe. Three different depths of the slot cut,  $a = 1.94, 2.20$  and  $2.81$ , were considered in the experiment. Fig. 10 shows the aluminium pipe with piezoceramic transducers and the location of the slot cut. Four equally-spaced Ferroperm Pz27 piezoceramic shear plates were bonded on the outer diameter surface at the left end of the pipe using conductive epoxy adhesive (Fig. 9). These piezoceramic shear plates generate shear forces in torsional direction of the pipe to induce the  $T(0,1)$  incident wave. In this study, it has been found that four piezoceramic shear plates are enough to generate the  $T(0,1)$  incident wave. The other piezoceramic shear plate was bonded at 0.3m away from the excitation location and it is used to measure the guided waves. The dimensions of each piezoceramic transducer are  $6 \times 6 \times 1 \text{ mm}^3$ . The density, Poisson's ratio and relative dielectric constant of the piezoceramic transducers are  $7700 \text{ kg/m}^3$ , 0.39 and 1800, respectively. The incident wave is excited by applying the equivalent torque generated by the piezoceramic transducers to the node of torsional motion ( $\theta$ ) in the SFEM model.



*Fig. 10 Piezoceramic transducers for generating incident  $T(0,1)$  wave and measurement, and the location of the slot cut in the aluminium pipe*

A 5-cycle Hanning windowed tone burst with centre frequency of 50kHz was generated by a computer-controlled function generator NI PIX-5412. A power amplifier (KROHN-HITE 7500) was used to amplify the signal from the function generator. The signal measured by the piezoceramic transducers was digitized by a data acquisition system (NI PIXe-5105). The sampling rate was 60MHz and the quality of the received signals was improved by averaging the measurements 500 times. A schematic diagram of the experiment setup is shown in Fig. 11.

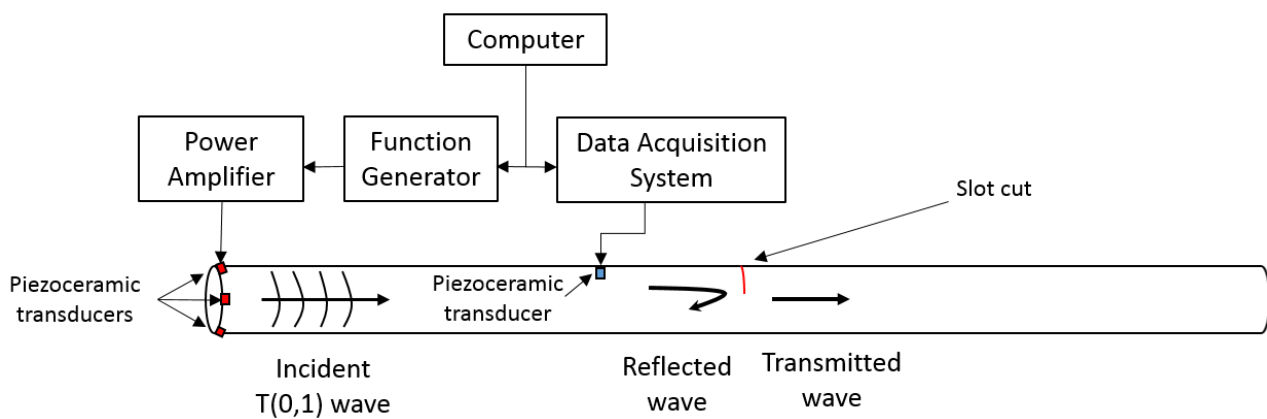


*Fig. 11 Schematic diagram of the experiment setup*

The guided wave signals simulated by the proposed time-domain SFEM was compared with the experimentally measured data. Fig. 12 shows the guided wave simulated by SFEM and the experimental data measured at 0.3m away from the excitation location. The red dashed line indicates the experimentally measured data, while the blue solid line presents the data simulated by the proposed SFEM. The incident wave T(0,1) interacts with the slot cut and generates T-T wave and mode converted T-F wave. The first captured wave packet is incident T(0,1). The second and third wave packets with small amplitude are T-T wave reflected from the slot cut and T-F wave induced due to mode conversion effect at the slot cut. The fourth wave packet is the T-T wave generated from the slot cut. It propagates to the left pipe end and then reflects back to the measurement point. The last wave packet is the incident T(0,1) wave reflected back from the right pipe end. There is good

agreement between the results simulated by the SFEM and experimental data for all three different depths of slot cuts. This shows the proposed time-domain SFEM and the cracked element are able to accurately predict the incident torsional wave, and scattered waves and mode converted wave due to the slot cut.

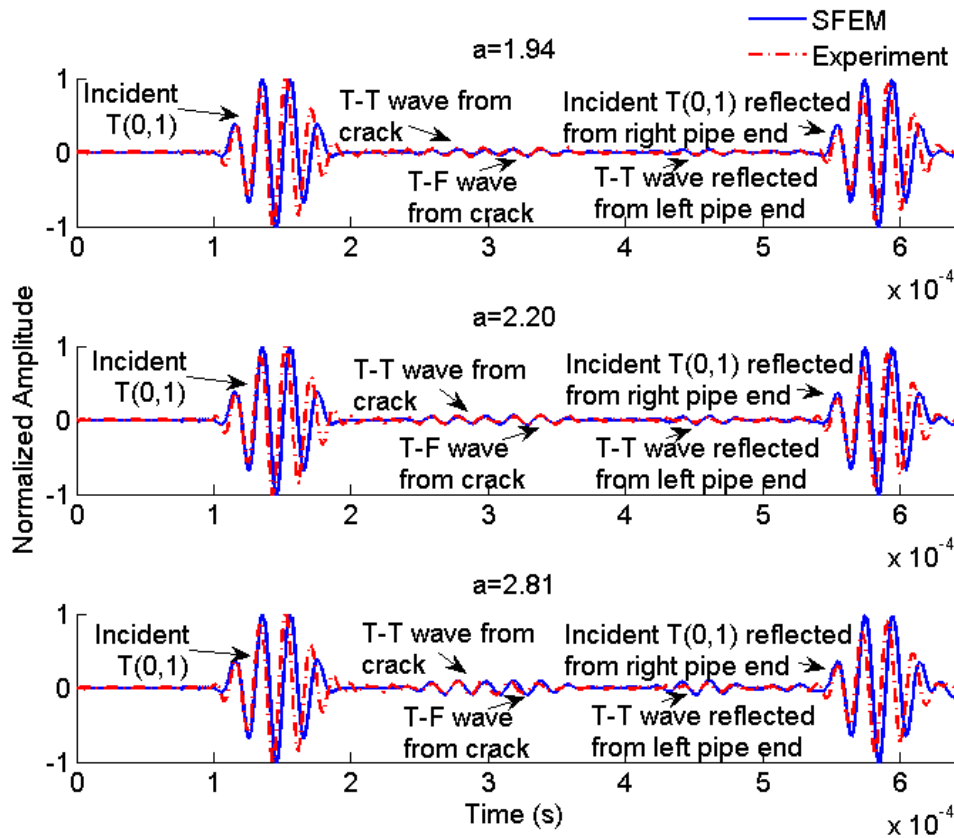
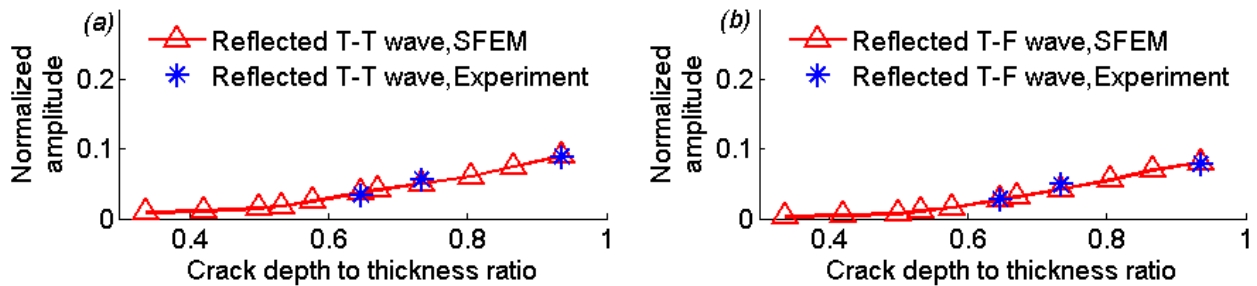


Fig. 12 Guided wave signals simulated by time-domain SFEM and measured in experiment



*Fig. 13 Normalized amplitude of SFEM simulated and experimentally measured wave signals as a function of crack depth to thickness ratio for a) reflected T-T wave, and b) reflected T-F wave.*

The amplitudes of the reflected T-T wave and T-F wave are extracted from the measured time-domain signals shown Fig. 12 and they are plotted in Fig. 13. The SFEM results of the parametric studies with different crack depth to thickness ratios are shown in the same figure. Fig. 13 shows that there is good agreement between the amplitudes obtained by SFEM and experiment for different crack depths to thickness ratios.

## **6. Conclusion**

A time-domain SFEM has been presented to simulate the torsional guided wave propagation, scattering and mode conversion at cracks in pipes. The proposed time-domain SFEM has three DoFs at each node, which is developed based on elementary rod theory and Timoshenko beam theory. A cracked element has been proposed to simulate the scattering and mode conversion when the guided wave interacts with the cracks in pipes. 3D finite element model has been used to validate the proposed time-domain SFEM and the cracked element. A series of parametric studies has been carried out to investigate the scattering and mode conversion effect of the torsional guided waves at different depths of the cracks. Experimental studies have been carried out to further verify the proposed SFEM method and the cracked element. The results have shown that the time-domain SFEM with the proposed cracked element is able to accurately predict the torsional wave propagation, scattering and mode conversion effect at the cracks in pipes. The results have shown that the reflected and transmitted wave amplitudes are sensitive to the change of the crack depth. The results of this study have gained physical insights into the torsional guided wave propagation, scattering and mode conversion at the cracks in pipes. The findings can further support the developments of damage

detection techniques using torsional guided wave. Future research can extend the study to bent pipe and buried pipe.

## References

1. Clarke T, Cawley P. (2011). Enhancing the defect localization capability of a guided wave SHM system applied to a complex structure. *Structural Health Monitoring*, 10(3):247-259.
2. Mohseni, H., & Ng, C. T. (2019). Rayleigh wave propagation and scattering characteristics at debondings in fibre-reinforced polymer-retrofitted concrete structures. *Structural Health Monitoring*, 18(1), 303-317.
3. Carden, E. P. & Fanning, P. (2004). Vibration based condition monitoring: a review. *Structural Health Monitoring*, 3(4):355-377.
4. Ng, C. T. (2015). A two-stage approach for quantitative damage imaging in metallic plates using Lamb waves. *Earthquakes and Structures*, 8(4):821-841.
5. Zhou, C., Zhang, C., Su, Z., Yue, X., Xiang, J. & Li, G. (2017) Health monitoring of rail structures using guided waves and three-dimensional diagnostic image. *Structural Control and Health Monitoring*, 24:e1966.
6. Soleimanpour, R. & Ng, C. T. (2017). Locating delaminations in laminated composite beams using nonlinear guided wave. *Engineering Structures*, 131:207-219.
7. Zhou, W., Li, H., & Yuan, F. G. (2013). Guided wave generation, sensing and damage detection using in-plane shear piezoelectric wafers. *Smart Materials and Structures*, 23(1), 015014.
8. Miao, H., Huan, Q., Wang, Q., & Li, F. (2017). Excitation and reception of single torsional wave T (0, 1) mode in pipes using face-shear d24 piezoelectric ring array. *Smart Materials and Structures*, 26(2), 025021.
9. Mohseni, H., & Ng, C. (2017). Rayleigh wave for detecting debonding in FRP-retrofitted concrete structures using piezoelectric transducers. *Computers and Concrete*, 20(5):583-593.
10. Ng, C. T. (2015). On accuracy of analytical modeling of Lamb wave scattering at delaminations in multilayered isotropic plates. *International Journal of Structural Stability and Dynamics*, 15(08), 1540010.
11. Sun, F., Sun, Z., Chen, Q., Murayama, R., & Nishino H (2016). Mode conversion behavior of guided wave in a pipe inspection system based on a long waveguide. *Sensors*, 16(10):1737.



12. Ng, C. T., Mohseni, H., & Lam, H. F. (2018). Debonding detection in CFRP-retrofitted reinforced concrete structures using nonlinear Rayleigh wave. *Mechanical Systems and Signal Processing*. <https://doi.org/10.1016/j.ymssp.2018.02.027>
13. Mohabuth, M., Kotousov, A., & Ng C. T. (2016). Effect of uniaxial stress on the propagation of higher-order Lamb wave modes. *International Journal of Nonlinear Mechanics*, 86:104-111.
14. Kudela, P., Radzienski, M., Ostachowicz, W., & Yang, Z. (2018). Structural health monitoring system based on a concept of Lamb wave focusing by the piezoelectric array. *Mechanical Systems and Signal Processing*, 108:21-32
15. He, S., & Ng, C. T. (2017). Guided wave-based identification of multiple cracks in beams using a Bayesian approach. *Mechanical Systems and Signal Processing*, 84:324-345.
16. Galvagni, A., & Cawley, P. (2011). The reflection of guided waves from simple supports in pipes. *The Journal of the Acoustical Society of America*, 129(4):1869-1880.
17. Cho, H., & Lissenden, C. (2012). Structural health monitoring of fatigue crack growth in plate structures with ultrasonic guided waves. *Structural Health Monitoring*, 11(4):393-404.
18. Yang, Y., Ng, C. T., Kotousov, A., Sohn, H., & Lim, H. J. (2018). Second harmonic generation at fatigue cracks by low-frequency Lamb waves: experimental and numerical studies. *Mechanical Systems and Signal Processing*, 99:760-773.
19. Yang, Y., Ng, C. T. & Kotousov, A. (2018). Influence of crack opening and incident wave angle on second harmonic generation of Lamb waves. *Smart Materials and Structures*, 27:055013.
20. Nagy, P. B., Simonetti, F., & Instanes, G. (2014). Corrosion and erosion monitoring in plates and pipes using constant group velocity Lamb wave inspection. *Ultrasonics*, 54(7):1832-1841.
21. Ahmad, R., Banerjee, S., & Kundu, T. (2008). Pipe Wall Damage Detection in Buried Pipes Using Guided Waves. *Journal of Pressure Vessel Technology*, 131(1):011501.
22. Angani, C., Park, D., Kim, C., Leela, P., Kishore, M. & Cheong, Y. (2011). Pulsed eddy current differential probe to detect the defects in a stainless steel pipe. *Journal of Applied Physics*, 109(7):07D348.
23. Rose, J. L., Sun, Z., Mudge, P. J., & Avioli, M. J. (2003). Guided Wave Flexural Mode Tuning and Focusing for Pipe Testing. *Materials Evaluation*, 61: 162-167.
24. Niu, X., Duan, W., Chen, H. P., & Marques, H. R. (2019). Excitation and propagation of torsional T (0, 1) mode for guided wave testing of pipeline integrity. *Measurement*, 131:341-348.
25. Løvstad, A. & Cawley, P. (2011). The reflection of the fundamental torsional guided wave from multiple circular holes in pipes. *NDT and E International*, 44:553-562.

26. Eybpoosh, M., Berges, M. & Noh, H. (2017). An energy-based sparse representation of ultrasonic guided-waves for online damage detection of pipelines under varying environmental and operational conditions. *Mechanical Systems and Signal Processing*, 82:260-278.
27. Willberg, C., Duczek, S., Vivar-Perez, J. M., & Ahmad, Z. A. B. (2015). Simulation methods for guided wave-based structural health monitoring: a review. *Applied Mechanics Reviews*, 67(1):010803.
28. Xu, F., Zhang, Y., Hong, W., Wu, K., & Cui, T. J. (2003). Finite-difference frequency-domain algorithm for modeling guided-wave properties of substrate integrated waveguide. *IEEE Transactions on Microwave Theory and Techniques*, 51(11):2221-2227.
29. Zhao, X. & Rose, J. (2003). Boundary element modeling for defect characterization potential in a wave guide. *International Journal of Solids and Structures*, 40:2645-2658.
30. Liu, G. (2002). A combined finite element/ strip element method for analyzing elastic wave scattering by cracks and inclusions in laminates. *Computational Mechanics*, 28:76-82.
31. Aryan, P., Kotousov, A., Ng, C. T., & Cazzolato, B. (2017). A model-based method for damage detection with guided waves. *Structural Control & Health Monitoring*, 24(3):e1884
32. Soleimanpour, R, & Ng, C. T. (2017). Higher harmonic generation of guided waves at delaminations in laminated composite beams. *Structural Health Monitoring*, 16(4):400-417.
33. Kim, Y., Ha, S., & Chang, F. K. (2008). Time-domain spectral element method for built-in piezoelectric-actuator-induced lamb wave propagation analysis. *AIAA journal*, 46(3), 591-600.
34. He, S, & Ng, C. T. (2016). A probabilistic approach for quantitative identification of multiple delaminations in laminated composite beams using guided waves. *Engineering Structures*, 127(15):602-614.
35. Seriani, G. Z., & Priolo, E. (1994). Spectral element method for acoustic wave simulation in heterogeneous media. *Finite Elements in Analysis and Design*, 16(3):337-348.
36. Dauksher, W., & Emery, A. F. (1999). An evaluation of the cost effectiveness of Chebyshev spectral and p-finite element solutions to the scalar wave equation. *International journal for numerical methods in engineering*, 45(8):1099-1113.
37. Willberg, C., Duczek, S., Perez, J. V., Schmicker, D., & Gabbert, U. (2012). Comparison of different higher order finite element schemes for the simulation of Lamb waves. *Computer Methods in Applied Mechanics and Engineering*, 241:246-261.
38. Duczek, S., Willberg, C., Schmicker, D., & Gabbert, U. (2012). Development, validation and comparison of higher order finite element approaches to compute the propagation of Lamb waves efficiently. *Key Engineering Materials*, 518:95-105.

39. Ostachowicz, W., Kudela, P., Krawczuk, M., & Zak, A. (2011). *Guided waves in structures for SHM: the time-domain spectral element method*. John Wiley & Sons.
40. Petyt, M. (2010). *Introduction to finite element vibration analysis*. Cambridge: Cambridge University Press.
41. Rucka, M. (2010). Experimental and numerical study on damage detection in an L-joint using guided wave propagation. *Journal of Sound and Vibration*, 329:1760-1779.
42. Doyle, J. F. (1989). *Wave propagation in structures*. Springer, New York, NY.
43. Reddy, J. N. (2006). *An introduction to the infinite element method*. New York: McGraw-Hill.
44. Rucka, M. (2010). Experimental and numerical studies of guided wave damage detection in bars with structural discontinuities. *Archive Applied Mechanics*, 80:1371-1390.
45. He, S., & Ng, C. T. (2017). Modelling and analysis of nonlinear guided waves interaction at a breathing crack using time-domain spectral finite element method. *Smart Materials and Structures*, 26:085002.
46. Kudela, P., Krawczuk, M. & Ostachowicz, W. (2006). Wave propagation modelling in 1D structures using spectral finite elements. *Journal of Sound and Vibration*, 300:88-100.
47. Tada, H., Paris, P., & Irwin, G. (2000). *The analysis of cracks handbook*. New York: ASME Press, 2, 1.
48. Ostachowicz, W., & Krawczuk, M. (1992). Coupled torsional and bending vibrations of a rotor with an open crack. *Archive of Applied Mechanics*, 62(3):191-2001.
49. Darpe, A. K., Gupta, K., & Chawla, A. (2004). Coupled bending, longitudinal and torsional vibrations of a cracked rotor. *Journal of Sound and Vibration*, 269(1-2):33-60.
50. Cowper, G. R. (1966). The shear coefficient in Timoshenko's beam theory. *Journal of Applied Mechanics*, 33(2):335-340.
51. Alleyne, D. N., Vogt, T. & Cawley, P. (2009). The choice of torsional or longitudinal excitation in guided wave pipe inspection. *Insight-Non-Destructive Testing and Condition Monitoring*, 51(7):373-377.
52. Pavlakovic, B Lowe, M. J. S. (2003). *DISPERSE: A System for Generating Dispersion Curves, User's Manual Version 2.0.16B*, Imperial College.
53. Yang, Y., Ng, C. T., Kotousov, A. (2019). Second harmonic generation of guided wave at crack-induced debonding in FRP-strengthened metallic plates. *International Journal of Structural Stability and Dynamics*, 19(1):1940006.
54. Aryan, P., Kotousov, A., Ng, C. T., & Widly, S. (2016). Reconstruction of baseline time-trace under changing environmental and operational cnditions. *Smart Materials and Structures*, 25:035018.